

**Electromagnetic Interference Shielding by
Transparent Graphene/Nickel Mesh Films**Van Viet Tran, Duc Dung Nguyen, An T. Nguyen, Mario
Hofmann, Ya-Ping Hsieh, Hung-Chih Kan, and Chia Chen Hsu*ACS Appl. Nano Mater.*, **Just Accepted Manuscript** • DOI: 10.1021/acsanm.0c01076 • Publication Date (Web): 01 Jul 2020

Downloaded from pubs.acs.org on July 2, 2020

Just Accepted

"Just Accepted" manuscripts have been peer-reviewed and accepted for publication. They are posted online prior to technical editing, formatting for publication and author proofing. The American Chemical Society provides "Just Accepted" as a service to the research community to expedite the dissemination of scientific material as soon as possible after acceptance. "Just Accepted" manuscripts appear in full in PDF format accompanied by an HTML abstract. "Just Accepted" manuscripts have been fully peer reviewed, but should not be considered the official version of record. They are citable by the Digital Object Identifier (DOI®). "Just Accepted" is an optional service offered to authors. Therefore, the "Just Accepted" Web site may not include all articles that will be published in the journal. After a manuscript is technically edited and formatted, it will be removed from the "Just Accepted" Web site and published as an ASAP article. Note that technical editing may introduce minor changes to the manuscript text and/or graphics which could affect content, and all legal disclaimers and ethical guidelines that apply to the journal pertain. ACS cannot be held responsible for errors or consequences arising from the use of information contained in these "Just Accepted" manuscripts.

Electromagnetic Interference Shielding by Transparent Graphene/Nickel Mesh Films

Van Viet Tran^a, Duc Dung Nguyen^a, An T. Nguyen^a, Mario Hofmann^b, Ya-Ping Hsieh^c, Hung-Chih Kan^a, and Chia-Chen Hsu^{a,*}

^a Department of Physics, National Chung Cheng University, Ming Hsiung, Chia Yi 621, Taiwan

^b Department of Physics, National Taiwan University, Taipei 10617, Taiwan

^c Institute of Atomic and Molecular Sciences, Academia Sinica, National Taiwan University, Taipei, 106, Taiwan

* phycch@ccu.edu.tw

ABSTRACT: In this work, we present efficient, robust, and transparent electromagnetic interference (EMI) shielding by a hybrid material comprised of a nickel (Ni) mesh and a conformal graphene coating. We demonstrate that a 20 nm thick graphene/Ni hybrid-mesh can provide EMI shielding effectiveness (SE) exceeded 12.1 dB (~ 93.6% power attenuation) in the decimeter band while retaining a high visible transmittance of ~ 83%. Its maximum achieved SE value was 26.6 dB (~ 99.5% power attenuation) at 0.75 GHz. Furthermore, the thicker Ni-mesh exhibited a higher EMI SE. Compared to conventional Ni-mesh, the hybrid-mesh exhibits a higher SE and a greatly improved corrosion resistance. The graphene coating is directly grown on Ni-mesh via rapid annealing of solid carbon precursors under low vacuum. Scalable fabrication of the mesh was achieved by a self-formed TiO₂ crack network template. Our results not only provide a promising material for high-performance EMI shielding in optoelectronics devices but also enable applications of EMI shielding in harsh environment.

KEYWORDS: graphene/nickel mesh, EMI shielding films, anti-corrosive conductors, graphene transparent conductors, low vacuum annealing.

I. INTRODUCTION

The massive use of wireless communications in daily life such as television, radio, cell phones, and mobile electronics produces many unwanted electromagnetic (EM) signals in the environment that may cause noise to electronic devices or even becomes hazardous to human health [1-5]. Thus, the need of electromagnetic interference (EMI) shielding is rising as an imperative issue. Generally, an effective EMI shielding material is dominated by three main functions: reflection, absorption, and multi-reflection [6]. Reflection of EM wave usually occurs at the surface of conductive materials and it is related to the relative impedance mismatch between the shield surface and the propagating wave. When EM wave goes inside the material, the absorption loss occurs because the currents induced in the materials produce ohmic losses and heating of the material. Both the reflection and the absorption performance of the EMI shielding materials are dependent on the high electrical conductivity. Multi-reflection is attributed to the EM wave trapped between two boundaries due to multiple reflection [7, 8]. Recently, various high-performance EMI shielding materials, such as nanofibers [9-11], carbon-based materials [12-15], transparent materials [16, 17], etc., have been studied. Among these EMI shielding materials, the transparent EMI shielding is very important for optoelectronic devices. High optical transmittance and strong EMI shielding effectiveness (SE) are two main requirements of EMI shielding to ensure unobstructed optical detection

as well as absolute isolation from unwanted electromagnetic signals for a variety of optoelectronic devices and components, e.g., observation windows, electronic displays, mobile communication devices, space exploration facilities, air gapped systems, and medical equipment, etc. [18-20].

To realize transparent EMI shielding, various materials have been investigated such as transparent conductive coatings, ultra-thin metal films, metallic meshes, and carbon-based materials [21-24]. Continuous conductive thin films, such as indium tin oxide (ITO) have only shown moderate attenuation of EM waves [25] at suitable transparencies. Graphene coatings exhibit superior electrical conductivity, flexibility and high transmittance and graphene-based materials have attracted significant attention for EMI shielding [26-28]. However, it possesses only a low EMI SE of 2.27 dB per layer over the frequency range of 2.2–7 GHz [29] with an optical absorption of 2.3%. A promising alternative is the use of hierarchically structured conducting materials which exhibit openings that are large compared to the wavelength of light but small in comparison to those of EM interference bands. Achieving such ordering on the micrometer scale, however, is challenging for randomly aligned nanostructures, such as Ag nanowires, carbon nanofibers, and carbon nanotubes, especially over large scale. Recently, conductive metal meshes (MM) have demonstrated large area EMI shielding with high visible transparency and good attenuation [24, 30, 31]. These structures are promising for high-performance transparent EMI shielding with broadband transparency from ultraviolet to near-infrared bands. To enable large scale integration of MM EMI shielding, low-cost fabrication from abundant materials have to be employed. Unfortunately, suitable low-cost source metals are environmentally unstable and the EMI shielding efficiency deteriorates quickly with time [32, 33].

We here present a hybrid material composed of graphene and MM for environmentally stable, transparent EMI shielding. Our approach is based on a scalably producible random network of nickel (Ni) mesh whose surface is conformally coated with graphene by a chemical vapor deposition process via rapid thermal annealing of solid carbon precursors. The 20 nm thick hybrid-mesh can provide EMI shielding effectiveness (SE) over 12.1 dB (~ 93.6% power attenuation) in the decimeter band while retaining a high visible transmittance of ~ 83%. Its maximum achieved SE value was 26.6 dB (~ 99.5% power attenuation) at 0.75 GHz. Furthermore, the thicker Ni-mesh exhibited a higher EMI SE. The long-term stability of our hybrid is significantly enhanced over conventional MMs due to the anti-corrosion properties of graphene [34, 35]. Our results provide a route towards enhancing the stability and scalability of metal mesh EMI shielding making them ideally suited for future applications in harsh environment.

II. EXPERIMENTAL SECTION

Preparation of TiO₂ cracked film. First, the TiO₂ suspension was synthesized by mixing the solution of DI water (0.5 ml), ethanol (2 ml), acetic acid (4 ml) (99%, Kermel, China) and titanium (IV) ethoxide (0.5 ml) (97%, Sigma – Aldrich) under continuous stirring (300 rpm) for 2-3 hours. Next, a 2.5×2.5 cm² cleaned quartz substrate was coated with the TiO₂ suspension by drop-coating. After few minutes, an interconnected crack layer was spontaneously formed during the evaporation of the solvents in air at room temperature due to its particle packing and volume shrinkage properties [36, 37].

Fabrication of hybrid-mesh. The cracked film on the quartz substrate was loaded into the vacuum chamber of a thermal evaporator, where the Ni was deposited. The TiO₂ template was then washed away by acetone solution under ultrasonication to leave only the Ni-mesh on the substrate. Finally, the graphene was directly coated on the Ni-mesh with solid carbon precursor via a rapid thermal annealing approach as reported in previous works [34, 38, 39]. In this process, Ni-mesh samples and cellulose acetate (CA) (C045A047A, Advantec) were first loaded into the sample container of an infrared lamp annealing system (Mila 5000, Ulvac). Subsequently, the sample was annealed at the desired temperatures for 8 min at a vacuum level of 0.6 Pa with a heating rate of 10 °C/s. The sample was then cooled to room temperature.

Characterizations. The morphologies and dimensions of the self-cracked TiO₂ film, Ni-mesh, and hybrid-mesh samples were examined by optical microscopy (OM, Hamlet MH101), atomic force microscopy (AFM, XE70), and scanning electron microscopy (SEM, Hitachi, S-3000H). The crystallographic and layered structures of the graphene coated Ni-mesh sample was investigated by Raman spectroscopy (Horiba, XploRA ONE). The sheet resistances of the samples were measured using a four-point probe instrument at room temperature. The visible transmittance was measured using an UV-Vis spectrometer (Agilent). The Energy-dispersive X-ray spectroscopy (EDS) of the field emission scanning electron microscopy (JSM-6500F) was used to examine the elemental composition of the graphene-mesh. The EM shielding efficiency was measured in the decimeter band using an antenna system with a vector network analyzer (Keysight E5061B). All measurements were calibrated with a quartz substrate. The Tafel plots, the logarithm of the current density (log (*i*)) versus the electrode potential, were recorded with a Jiehan 5600 electrochemical workstation. Contact angle was determined at room temperature using a CAM110 contact angle meter (Creating-nanotech, Taiwan) using a 2 μL deionized water droplet.

III. RESULTS AND DISCUSSION

Figure 1 schematically illustrates the fabrication procedure of the graphene/nickel hybrid-mesh, including (1) drop coating of TiO₂ suspension on a quartz substrate to form a TiO₂ thin film atop of the substrate, (2) self-formation of interconnected cracks on the TiO₂ thin film, (3) deposition of Ni thin film, (4) lift-off the TiO₂ layer to get interconnected Ni-mesh, and (5) directly growing graphene on the Ni-mesh.

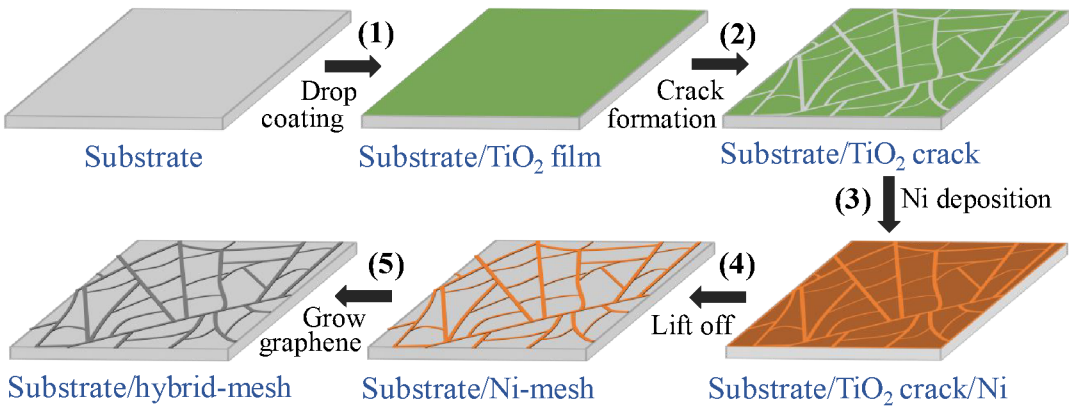


Figure 1. Schematic of the fabrication process of the hybrid material consisted of graphene and Ni-mesh

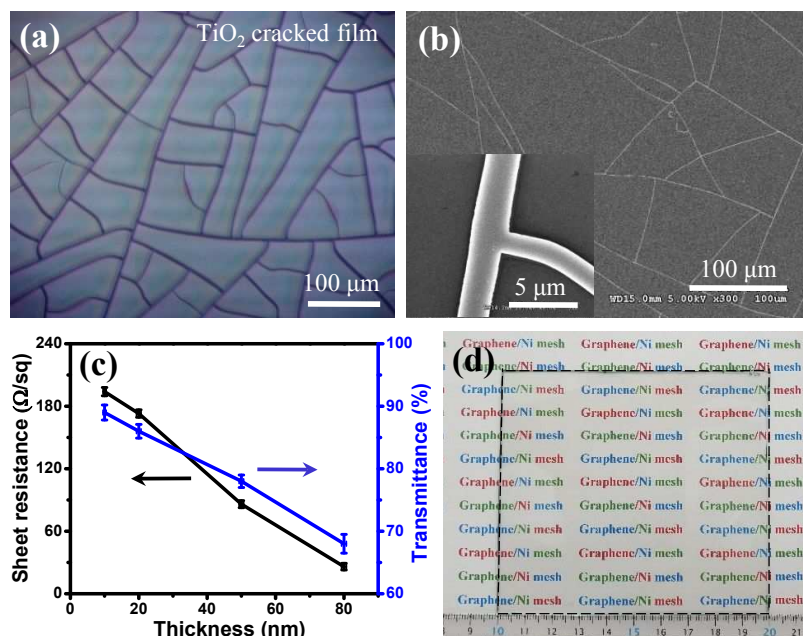


Figure 2. (a) Optical microscopy image of TiO₂ cracked film. (b) SEM image of Ni-mesh. (Inset: high magnification image of Ni wires (scale bar is 5 μm)). (c) Dependences of sheet resistance and visible transmittance on thickness of Ni-mesh. (d) Picture of 20 nm thick Ni-mesh film in large scale.

The chemical composition of the TiO₂ suspension was optimized for the highest transparency of the sample. An OM image of TiO₂ cracked film on a quartz substrate is shown in Figure 2a. It displays that the cracks are well-connected. An individual representative crack was characterized by AFM measurement. The typical depth and width of the crack are found to be around 0.6 μm and 1.52 μm, respectively, as shown in Figure S1. The SEM images (see Figure S2) of several random positions of TiO₂ crack film were chosen to determine the average of the crack width. The average of TiO₂ crack width is 1.891 μm. Figure 2b shows the SEM image of the Ni-mesh, which contains randomly distributed Ni wire networks with line spacing of about 40 - 120 μm. The inset shows a high magnification image of Ni wires. It is clear that the wires are well-connected and that their widths are about of 1 - 3 μm, which is compatible to the widths of the TiO₂ cracks shown in Figure 2a. The thickness of Ni-mesh was characterized by AFM measurement. Figure S3 displays the thickness of four Ni-mesh samples with the nominal Ni film thickness of 10 nm, 20 nm, 50 nm and 80 nm. The thicknesses of Ni-mesh were accurately controlled and repeatable, as indicated by error bars of the thicknesses shown in Figure 2c. The transmittance spectra of four Ni-mesh samples are presented in Figure S4. The transmittance of Ni-mesh can be estimated by Equation (1): $T = A + (1 - A)\exp\left(-t/\delta\right)$, where T is the optical transmittance; A is the non-Ni area fraction of the sample; δ is the skin depth of Ni; and t is the thickness of Ni. Figure S5 shows the transmittance at 550 nm of four Ni-mesh samples and a fitting curve according to Equation (1). It illustrates that the transmittance data fits well to the equation with fitting parameters $A = 0.675$ and $\delta = 36$ nm. The fitting value of δ is close to a theoretical calculation value of 23 nm [40]. The transmittance of each sample almost remains constant at wavelength range from 400 nm to 1000 nm. The transmittance at 550 nm of each sample was chosen as a representative transmission and its relation with sheet resistance as a function of thickness of Ni wire is shown in Figure 2c. The result reveals that both sheet resistance and transmittance decrease with the increase of Ni-mesh thickness. The 20 nm thick Ni-

mesh sample displays high visible transmittance ($\sim 86\%$), with sheet resistance ($\sim 173 \Omega/\text{sq.}$). Figure 2d presents a picture of a large size Ni-mesh sample ($10 \times 10 \text{ cm}^2$) with 20 nm thick Ni wires on a quartz substrate, which clearly demonstrates the good transparency of the Ni-mesh sample.

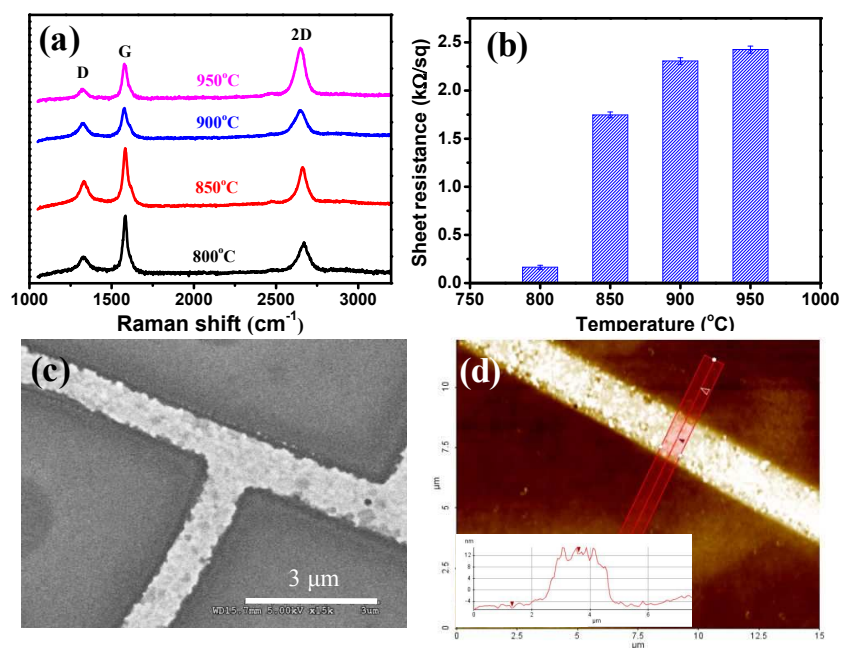


Figure 3. (a) Raman spectra of graphene grown at different temperatures. (b) Sheet resistance of hybrid-mesh grown at different temperatures. (c) SEM image and (d) AFM image of hybrid-mesh grown at 800 °C. The results of (a)-(d) were obtained by using a 20 nm thick of Ni-mesh.

The hybrid-mesh was fabricated on 20 nm thick Ni-mesh by directly growing graphene via rapid thermal annealing of cellulose acetate. Graphene was grown at annealing temperatures of 800, 850, 900, and 950 °C. The quality of graphene on the surface of the hybrid-mesh was characterized by Raman spectroscopy, as shown in Figure 3a and S6. The Raman spectra in Figure 3a are the average of several locations of the samples shown in Figure S6. As displayed in Figure 3a, all the hybrid-mesh samples contained the D peak at $\sim 1348 \text{ cm}^{-1}$, and two characteristic peaks of graphene; i.e., the G peak at $\sim 1580 \text{ cm}^{-1}$; and the 2D peak at $\sim 2704 \text{ cm}^{-1}$ [41, 42]. The presence of the D peak is due to defects or edges of graphene. The hybrid-mesh sample grown at 950 °C had the highest I_{2D}/I_G , i.e., intensity ratio of the 2D peak over the G peak (see Figure S7), indicating that its graphene layer number is the least [43]. For the samples grown at 800, 850, and 900 °C, few layers of graphene were obtained. In contrast, the sample grown at 950 °C had bilayer graphene [41, 43]. The surfaces of hybrid-meshes grown at temperature 850 – 950 °C were rough and discontinuous due to the melting and formation of islands of Ni during the annealing process. As illustrated in Figure S8, the surface roughness and discontinuity increased with the increase of annealing temperature, which is the main reason for the increase of sheet resistance of the hybrid-mesh samples grown at 850 – 950 °C (see Figure 3b). The sheet resistance of the hybrid-mesh sample grown at 800 °C was close to that of the bare Ni-mesh. Herein, we focus our investigation on the hybrid-mesh sample grown at 800 °C because its sheet resistance and surface roughness were much smaller than those of obtained at higher temperatures (850 – 950 °C) (see Figure 3b-d and S8). The fact that the 20 nm thickness of Ni-mesh can undergo annealing temperature up to 800 °C is proven by SEM and AFM images of the hybrid-mesh shown in Figure 3c

and 3d. The Ni wires were preserved after growing graphene. Figure S9a and S9b present the SEM images of the remaining graphene structure on the substrate after etching away Ni by FeCl_3/HCl (1M/1M) solution. From the SEM images, we confirmed that graphene was continuously grown on surface of Ni mesh. Furthermore, the EDS data (Figure S9c), acquired at the graphene position, reveals that Ni mesh was totally removed and graphene was still remained on the substrate. The strong signals of Si and O₂ elements are attributed to the substrate.

Figure 4a plots sheet resistance and optical transmittance of hybrid-mesh samples grown at 800 °C versus the thickness of Ni-mesh. The transmittance values were chosen at wavelength $\lambda = 550$ nm from the transmission spectra of hybrid-mesh samples shown in Figure S10a. Compared to the transmittances of the Ni-mesh shown in Figure 2c, the transmittances of hybrid-mesh samples were about 2 to 3% lower than those of Ni-mesh samples, which was mainly due to the deposition of carbon atoms onto the surface of the substrate (including the area outside of the Ni wires) during the thermal annealing process. This explanation is supported by the amorphous carbon feature of the Raman spectrum acquired at areas outside of Ni wires (see Figure S11) [44]. Figure S10b displays a good transparency picture of a hybrid-mesh film (2.5×2.5 cm²) obtained with 20 nm thick Ni wires on a quartz-glass substrate. Note that a larger size of hybrid-mesh film can be fabricated if a bigger furnace is used. All sheet resistances of hybrid-mesh samples were lower than those of pristine Ni-mesh samples except the one grown on 10 nm thick Ni-mesh. The deviation is due to the increase of surface roughness of Ni-mesh during the thermal annealing process (see Figure S12).

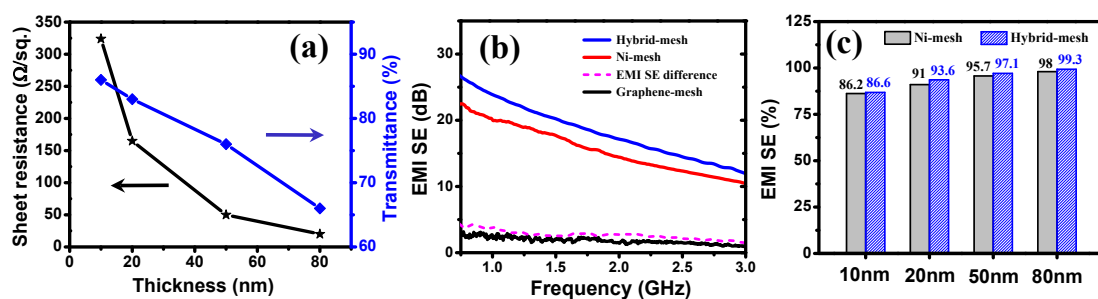


Figure 4: (a) Dependences of sheet resistance and transmittance of hybrid-mesh on the thickness of Ni-mesh used to grow graphene. (b) EMI SE (dB) spectra of hybrid-mesh and Ni-mesh, difference between the aforementioned two, and graphene-mesh (Ni etched away by FeCl_3/HCl (1M/1M) solution). (c) EMI SE (%) at 3 GHz of hybrid-mesh and Ni-mesh samples versus Ni-mesh thickness.

The EMI shielding efficiency (SE) is defined as the logarithmic ratio of the incident EMI power (P_i) and the transmitted EMI power (P_o) [31, 33], which represents the transmission coefficient (T_{EMI}) of a shielding material. Hence, $\text{SE (dB)} = -10 \log(P_o/P_i) = -10 \log(T_{\text{EMI}})$ and $\text{SE (\%)} = (1 - T_{\text{EMI}}) \times 100\%$. The EMI SE of the hybrid-mesh was measured by a system composed of a vector network analyzer, emitter and receiver antennas in the frequency range of 0.75 to 3 GHz. It lies in the decimeter band consisting of frequencies of television broadcasting, cell phones, GPS, and personal radio services such as Wi-Fi and Bluetooth.

The EMI SE spectra of hybrid-mesh and Ni-mesh samples with different thicknesses of Ni-mesh are shown in Figure S13. As shown, the EMI SE decreased with frequency, which is attributed to the decrease of reflection of high frequency microwave [24, 45]. The skin depth (δ) value of the 20 nm thick Ni-mesh was calculated using

the formula: $\delta = 1/\sqrt{\pi f \sigma \mu}$ [46], where f is the frequency; σ is electrical conductivity which was calculated by formula of $\sigma = (R \cdot t)^{-1}$ (where R is sheet resistance obtained by four-point probe measurement, t is thickness), and μ is the magnetic permeability of material with a relationship of $\mu = \mu_0 \mu_r$ ($\mu_0 = 4\pi \times 10^{-7}$ H/m and $\mu_r = 600$ is the relative magnetic permeability of nickel). The calculated result is plotted in Figure S14. It is clear that Ni-mesh thickness used in this work is much smaller than the skin depth. Therefore, the major EMI shielding mechanism is attributed to reflection loss [47]. Figure 4b shows the EMI SE (dB) spectra of hybrid-mesh, Ni-mesh, and graphene-mesh (Ni etched away by FeCl₃/HCl (1M/1M) solution); all of them are with 20nm thickness. As displayed, both bare Ni-mesh and hybrid-mesh samples exhibited high EMI SE. Particularly, the growth of graphene on the Ni-mesh increased the EMI SE about 1.5 to 4 dB, which is mainly contributed from the reflection loss of EM wave by the graphene coating. Figure 4b shows the EMI SE difference between hybrid-mesh and Ni-mesh versus frequency, which is very close to the EMI SE of the graphene-mesh. It indicates that the increase of the EMI SE of the hybrid-mesh is indeed contributed from the coating of graphene on surface of the Ni-mesh. The small discrepancy may be due to multi-reflection of EM wave between surfaces of graphene and Ni wire. The highest and lowest EMI SE obtained from the 20 nm thick hybrid-mesh were 26.6 dB (~99.5% power attenuation) at 0.75 GHz and 12.1 dB (~93.6% power attenuation) at 3 GHz, respectively. The EMI SE (dB) of all the samples at 3GHz, where the EMI SE of the samples was the smallest in the decimeter band, were chosen to represent their EMI SE (%) values. Figure 4c plots the EMI SE (%) of hybrid-mesh and the Ni-mesh samples versus Ni-mesh thickness. As illustrated, the thicker Ni-mesh thicknesses exhibit a higher EMI SE. Moreover, the growth of graphene on Ni-mesh above 10nm thickness indeed increased the EMI SE (%) compared to the unwanted decrease in light transmittance. This effect can be understood from the greater improvement in sheet resistance on EMI SE (%) [24]. The EMI shielding performance of the amorphous carbon thin film sample was measured (as shown in Figure S15). It is clear that the amorphous carbon thin film played an insignificant roll for EMI shielding. As shown in Figure 4a and 4c, the hybrid-mesh sample grown on the 20 nm thick Ni-mesh yielded high visible transmittance (~83%) and excellent EMI SE (~93.6% power attenuation). Furthermore, the 80 nm thick hybrid-mesh sample yielded the highest EMI SE (~99.3% power attenuation) at 3 GHz with an acceptable visible transmittance (~67%). In Table S1, the EMI shielding performance of the 20 nm thick hybrid mesh is compared to those of similar materials, which are comprised of metallic mesh and transferred monolayer graphene. As indicated, the EMI SE value obtained in this work is comparable to the results of similar materials [32, 33, 48]. However, those materials were fabricated using a complicated multi-step or graphene-transferred process.

Beside high optical transparency and excellent EMI shielding performances, the stability of shielding materials in harsh environment is also an important factor. The corrosion resistance of the hybrid-mesh was characterized in 0.1 M Na₂SO₄ solution. A potentiostat was used to record the Tafel plot, i.e., the logarithm of the current density (log (i)) vs. the electrode potential. To check the reproducibility of materials, the scan was repeated three times with a scan rate of 20 mV/s [34]. Figure 5a shows Tafel polarization curves of the 20 nm thick Ni-mesh before and after the growth of graphene at 800 °C measured in 0.1 M Na₂SO₄ solution. Tafel analysis was used to determine the corrosion current density (i_{corr}) and the corrosion potential (E_{corr}) from the intersection point of asymptotic lines of the polarization curves [49, 50]. Compared to the bare Ni-mesh, the hybrid-mesh exhibited a lower i_{corr} , while its E_{corr} was shifted toward larger positive potential (see Table 1). This implies the graphene coating acts an inhibitor to increase the corrosion resistance of Ni [50].

The corrosion rates (CR) of samples were calculated with the following formula [51]:

$$CR = \frac{K \times i_{corr} \times EW}{\rho \times A} \quad (2)$$

where K (corrosion rate constant) = 3272 mm per A per cm per year; EW (equivalent weight) = 29 g (for Ni); ρ (density) = 8.9 g/cm³ (for Ni); and A (sample area) = (0.44 cm²).

Table 1. The corrosion current density, the corrosion potential and corrosion rate of Ni-mesh and hybrid-mesh.

Sample	i_{corr} (A/cm ²)	E_{corr} (V vs. Ag/AgCl)	Corrosion rate (m/s)
Ni-mesh	2.772×10^{-7}	0.347	2.13×10^{-13}
Hybrid-mesh	8.785×10^{-8}	0.63	6.75×10^{-14}

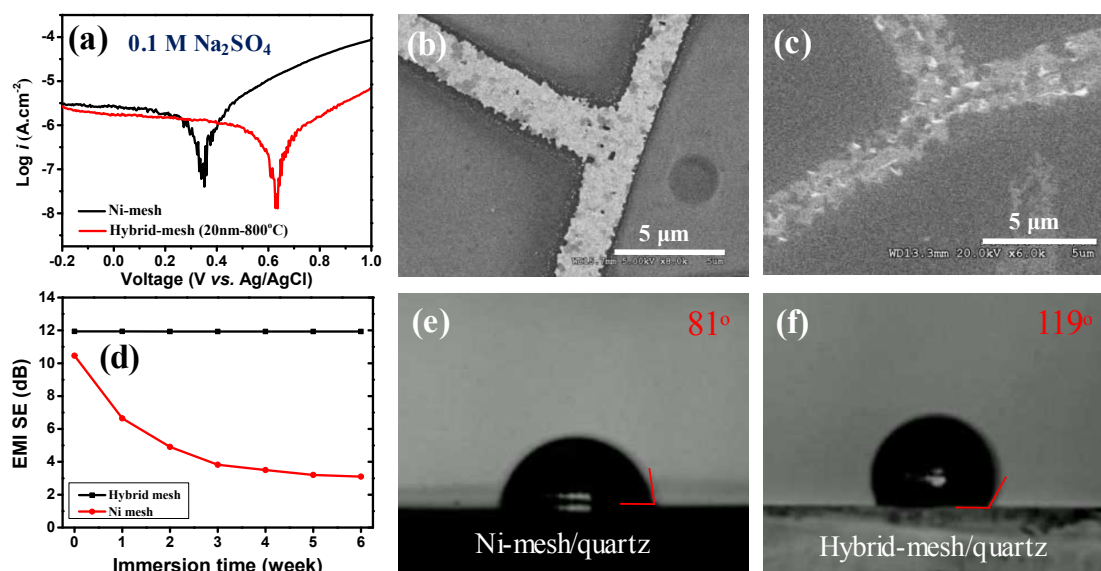


Figure 5: (a) Tafel plots of the Ni-mesh and hybrid-mesh samples. SEM image after anti-corrosion measurement (b) hybrid-mesh (c) Ni-mesh. (d) EMI SE versus immersion time in Na₂SO₄ 0.1M solution for the both Ni-mesh and the hybrid-mesh at frequency 3GHz. Contact angles of both (e) Ni-mesh, (f) hybrid-mesh. All the results shown in (a)-(f) were obtained by using a 20 nm thick of Ni-mesh.

As shown in Table 1, the corrosion rate of the hybrid-mesh was only 31% of the uncoated Ni-mesh. Furthermore, Raman spectra of the hybrid-mesh showed no change after the anti-corrosion measurement (see Figure S16). Figures 5b and 5c present SEM images of the hybrid-mesh and bare Ni-mesh after the anti-corrosion measurement, respectively. As displayed, the bare Ni-mesh was obviously corroded by the anodic oxidation reaction, $\text{Ni}^0 \rightarrow \text{Ni}^{2+} + 2\text{e}^-$, while the morphology of the hybrid-mesh was preserved. Figure 5d shows the time evolution of EMI SE at 3 GHz of the hybrid-mesh and the bare Ni-mesh during exposure to 0.1 M Na₂SO₄ solution for six weeks. As displayed, the hybrid-mesh only exhibited a slight change in EMI SE, suggesting the excellent corrosion protection of graphene. However, the EMI SE of the bare Ni-mesh exhibited a quick decay because of the oxidation of Ni wires. Moreover, the hybrid-mesh exhibited hydrophobic property with contact angle of 119° which is much higher than contact angle of the bare Ni-mesh (81°), (see Figure 5e and 5f). It reveals that the

graphene coated Ni-mesh can enhance the hydrophobicity and reduce the contact of sample with aqueous solutions.

IV. CONCLUSIONS

In conclusion, we presented a simple and robust approach to produce hybrid graphene/Ni mesh structures that combine high visible transparency with excellent microwave shielding performance and high corrosion resistance. Few-layer graphene was directly coated on Ni-mesh via rapid thermal annealing technique with solid carbon precursor. EMI SE and the visible transmittance of hybrid-mesh were investigated. The hybrid-mesh exhibited excellent performance of EMI SE (from 86.6 % to 99.3%) at the smallest value in the decimeter band and high visible transmittance (from 67% to 86%) of random pattern. In addition, the wrap of graphene around the surface of Ni wires not only slightly increases the shielding effectiveness but also greatly improves the corrosion resistance of the hybrid-mesh. Raman spectra of graphene after anti-corrosion measurement are similar to the samples before, indicating the good stability of the graphene coating in the corrosion environment. Moreover, long term stability of the hybrid-mesh was also investigated by immersing the sample in 0.1 M Na₂SO₄ solution for 6 weeks. The EMI SE results barely change, indicating that graphene acts as an impermeable barrier against the diffusion of corrosive agents. This study not only provides a promising material for high-performance EMI shielding in optoelectronics devices but also enable applications of EMI shielding in harsh environment.

V. ASSOCIATED CONTENT

Supporting Information

AFM profile of a single TiO₂ crack, SEM images of TiO₂ crack film, AFM profile of Ni thicknesses, transmission spectra of Ni-mesh samples, fitting curve of transmittance vs. Ni thickness, Raman spectra of samples, the intensity ratio I_{2D}/I_G of graphene, SEM images and AFM profile of samples after graphene growth, SEM images of graphene and EDS analysis acquired at the area of graphene, transmission spectra of hybrid-mesh, picture of a hybrid-mesh film, Raman spectrum at area outside of Ni wire, SEM image of 10 nm thick Ni-mesh coated graphene at 800 °C, EMI SE spectra of hybrid-mesh and Ni-mesh, skin depth of Ni-mesh samples, EMI SE of amorphous carbon film, Raman spectra of hybrid-mesh before and after anti-corrosion measurement, performance of different graphene/metallic mesh hybrid materials.

VI. AUTHOR INFORMATION

Corresponding Author

*E-mail: phycch@ccu.edu.tw. Phone: +886-5-2720411 x66305.

ORCID

Duc Dung Nguyen: 0000-0002-4997-7379

An T. Nguyen: 0000-0003-4988-5965

Mario Hofmann: 0000-0003-1946-2478

Ya-Ping Hsieh: 0000-0002-6065-751X

Chia-Chen Hsu: 0000-0002-3014-8829

Notes

The authors declare no competing financial interest.

VII. ACKNOWLEDGMENTS

This study was financially supported by the Ministry of Science and Technology (MOST) of the Republic of China (Taiwan) (MOST 104-2112-M-194-002-MY3 and MOST 107-2112-M-194-011-MY3).

VIII. REFERENCES

- (1) Chung, D. D. L. Electromagnetic Interference Shielding Effectiveness of Carbon Materials. *Carbon* **2001**, *39*, 279–285.
- (2) Ding, D.; Wang, Y.; Li, X.; Qiang, R.; Xu, P.; Chu, W.; Han, H.; Du, Y. Rational Design of Core-shell Co@C Microspheres for High-Performance Microwave Absorption. *Carbon* **2017**, *111*, 722-732.
- (3) Bhargavi, K.; Balachandrudu, K.; Nageswar, P. Mobile Phone Radiation Effects on Human Health. *International Journal of Computational Engineering Research* **2013**, *03*, 196-203.
- (4) Christopher, B.; Mary, Y. S.; Khandaker, M. U.; Bradley D. A.; Chew, M. T.; Jojo, P. J. Effects of Mobile Phone Radiation on Certain Hematological Parameters. *Radiation Physics and Chemistry* **2020**, *166*, 108443.
- (5) Christopher, B.; Mary, Y. S.; Khandaker, M. U.; Jojo, P. J. Empirical Study on Specific Absorption Rate of Head Tissues due to Induced Heating of 4G Cell Phone Radiation. *Radiation Physics and Chemistry* **2020**, 108910.
- (6) Ji, H.; Zhao, R.; Zhang, N.; Jin, C.; Lu, X.; Wang, C. Lightweight and Flexible Electrospun Polymer Nanofiber/Metal Nanoparticle Hybrid Membrane for High-Performance Electromagnetic Interference Shielding. *NPG Asia Materials* **2018**, *10*, 749–760.
- (7) Shukla, V. Review of Electromagnetic Interference Shielding Materials Fabricated by Iron Ingredients. *Nanoscale Adv.* **2019**, *1*, 1640.
- (8) Saini, P.; Arora, M. Microwave Absorption and EMI Shielding Behavior of Nanocomposites Based on Intrinsically Conducting Polymers, Graphene and Carbon Nanotubes. *In New Polymers for Special Applications*; Gomes, A. D., Ed.; InTech: Rijeka, Croatia, **2012**; DOI: 10.5772/48779.
- (9) Huang, L.; Li, J.; Li, Y.; He, H.; Yuan, Y. Lightweight and Flexible Hybrid Film Based on Delicate Design of Electrospun Nanofibers for High-Performance Electromagnetic Interference Shielding. *Nanoscale* **2019**, *11*, 8616.

(10) Zhou, B.; Zhang, Z.; Li, Y.; Han, G.; Feng, Y.; Wang, B.; Zhang, D.; Ma, J.; Liu, C. Flexible, Robust and Multifunctional Electromagnetic Interference Shielding Film with Alternating Cellulose Nanofiber and MXene Layers. *ACS Appl. Mater. Interfaces* **2020**, *12*, 4895–4905.

(11) Li, H.; Jensen, M.; Wang, N.; Chen, Y.; Gao, Y.; Chen, X.; Li, X. CuxS/PAN 3D Nanofiber Mats as Ultra-Lightweight and Flexible Electromagnetic Interference Shielding Materials. *Macromol. Mater. Eng.* **2019**, 1900482.

(12) Huang, L.; Li, J.; Wang, Z.; Li, Y.; He, X.; Yuan, Y. Microwave Absorption Enhancement of Porous C@CoFe₂O₄ Nanocomposites Derived from Eggshell Membrane. *Carbon* **2019**, *143*, 507-516.

(13) Lai, D.; Chen, X.; Liu, X.; Wang, Y. Flexible Poly(vinyl alcohol)/Reduced Graphene Oxide Coated Carbon Composites for Electromagnetic Interference Shielding. *ACS Appl. Nano Mater.* **2018**, *1*, 5854–5864.

(14) Vallés, C.; Zhang, X.; Cao, J.; Lin, F.; Young, R. J.; Lombardo, A.; Ferrari, A. C.; Burk, J.; Mülhaupt, R.; Kinloch, I. A. Graphene/Polyelectrolyte Layer-by-Layer Coatings for Electromagnetic Interference Shielding. *ACS Appl. Nano Mater.* **2019**, *2*, 5272–5281.

(15) Kumar, R.; Macedo, W. C. Jr.; Singh, R. K.; Tiwari, V. S.; Constantino, C. J. L.; Matsuda, A.; Moshkalev, S. A. Nitrogen–Sulfur Co-Doped Reduced Graphene Oxide-Nickel Oxide Nanoparticle Composites for Electromagnetic Interference Shielding. *ACS Appl. Nano Mater.* **2019**, *2*, 4626–4636.

(16) Kim, D. H.; Kim, Y.; Kim, J. W. Transparent and Flexible Film for Shielding Electromagnetic Interference. *Materials and Design* **2016**, *89*, 703–707.

(17) Kumar, P.; Reddy, P. V.; Choudhury, B.; Chowdhury, P.; Barshilia, H. C. Transparent Conductive Ta/Al/Ta-Grid Electrode for Optoelectronic and Electromagnetic Interference Shielding Applications. *Thin Solid Films* **2016**, *612*, 350–357.

(18) Jung, J.; Lee, H.; Ha, I.; Cho, H.; Kim, K. K.; Kwon, J.; Won, P.; Hong, S.; Ko, S. H. Highly Stretchable and Transparent Electromagnetic Interference Shielding Film Based on Silver Nanowire Percolation Network for Wearable Electronics Applications. *ACS Appl. Mater. Interfaces* **2017**, *9*, 44609–44616.

(19) Lin, S.; Wang, H.; Wu, F.; Wang, Q.; Bai, X.; Zu, D.; Song, J.; Wang, D.; Liu, Z.; Li, Z.; Tao, N.; Huang, K.; Lei, M.; Li, B.; Wu, H. Room-Temperature Production of Silver-Nanofiber Film for Large-Area, Transparent and Flexible Surface Electromagnetic Interference Shielding. *NPJ Flexible Electronics* **2019** 3:6.

(20) Kim, S.; Oh, J. S.; Kim, M. G.; Jang, W.; Wang, M.; Kim, Y.; Seo, H. W.; Kim, I. C.; Lee, J. H.; Lee, Y.; Nam, J. D. Electromagnetic Interference (EMI) Transparent Shielding of Reduced Graphene Oxide (RGO)

- Interleaved Structure Fabricated by Electrophoretic Deposition. *ACS Appl. Mater. Interfaces* **2014**, *6*, 17647–17653.
- (21) Jia, L. C.; Yan, D. X.; Liu, X.; Ma, R.; Wu, H. Y.; Li, Z. M. Highly Efficient and Reliable Transparent Electromagnetic Interference Shielding Film. *ACS Appl. Mater. Interfaces* **2018**, *10*, 11941–11949.
- (22) Erdogan, N.; Erden, F.; Astarlioglu, A. T.; Ozdemir, M.; Ozbay, S.; Aygun, G.; Ozyuzer, L. ITO/Au/ITO Multilayer Thin Films on Transparent Polycarbonate with Enhanced EMI Shielding Properties. *Curr. Appl. Physics* **2020**, *20*, 489–497.
- (23) Al-Saleh, M. H.; Saadeh, W. H.; Sundararaj, U. EMI Shielding Effectiveness of Carbon Based Nanostructured Polymeric Materials: A Comparative Study. *Carbon* **2013**, *60*, 146 – 156.
- (24) Wang, H.; Lu, Z.; Liu, Y.; Tan, J.; Ma, L.; Lin, S. Double-Layer Interlaced Nested Multi-Ring Array Metallic Mesh for High-Performance Transparent Electromagnetic Interference Shielding. *Optics Letters* **2017**, *42*, 1620 -1623.
- (25) Huang, J. L.; Yau, B. S.; Chen, C. Y.; Lo, W. T.; Lii, D. F. The Electromagnetic Shielding Effectiveness of Indium Tin Oxide Films. *Ceramics International* **2001**, *27*, 363–365.
- (26) Batrakov, K.; Kuzhir, P.; Maksimenko, S.; Paddubskaya, A.; Voronovich, S.; Lambin, P.; Kaplas, T.; Svirko, W. Flexible Transparent Graphene/Polymer Multilayers for Efficient Electromagnetic Field Absorption. *Scientific Report* **2014**, *4*, 7191.
- (27) Lu, Z.; Ma, L.; Tan, J.; Wang, H.; Ding, X. Transparent Multi-Layer Graphene/Polyethylene Terephthalate Structures with Excellent Microwave Absorption and Electromagnetic Interference Shielding Performance. *Nanoscale* **2016**, *8*, 16684–16693.
- (28) Kumar, P.; Shahzad, F.; Hong, S. M.; Koo, C. M. A Flexible Sandwich Graphene/Silver Nanowires/Graphene Thin Film for High-Performance Electromagnetic Interference Shielding. *RSC Adv.* **2016**, *6*, 101283.
- (29) Hong, S. K.; Kim, K. Y.; Kim, T. Y.; Kim, J. H.; Park, S. W.; Kim, J. H.; Cho, B. J. Electromagnetic Interference Shielding Effectiveness of Monolayer Graphene. *Nanotechnology* **2012**, *23*, 455704.
- (30) Jiang, Z. Y.; Huang, W.; Chen, L. S.; Liu, Y. H. Ultrathin, Lightweight, and Freestanding Metallic Mesh for Transparent Electromagnetic Interference Shielding. *Optics Express* **2019**, *27*, 24194–24206.
- (31) Han, Y.; Lin, J.; Liu, Y.; Fu, H.; Ma, Y.; Jin, P.; Tan, J. Crackle Template Based Metallic Mesh with Highly Homogeneous Light Transmission for High-Performance Transparent EMI Shielding. *Scientific Reports* **2016**, *6*, 25601.

(32) Ma, L.; Lu, Z.; Tan, J.; Liu, J.; Ding, X.; Black, N.; Li, T.; Gallop, J.; Hao, L. Transparent Conducting Graphene Hybrid Films to Improve Electromagnetic Interference (EMI) Shielding Performance of Graphene. *ACS Appl. Mater. Interfaces* **2017**, *9*, 34221–34229.

(33) Han, Y.; Liu, Y.; Han, L.; Lin, J.; Jin, P. High-Performance Hierarchical Graphene/Metal-Mesh Film for Optically Transparent Electromagnetic Interference Shielding. *Carbon* **2017**, *115*, 34–42.

(34) Nguyen, A. T.; Lai, W. C.; To, B. D.; Nguyen, D. D.; Hsieh, Y. P.; Hofmann, M.; Kan, H. C.; Hsu, C. C. Layer Control of Tubular Graphene for Corrosion Inhibition of Nickel Wires. *ACS Appl. Mater. Interfaces* **2017**, *9*, 22911–22917.

(35) Hsieh, Y. P.; Hofmann, M.; Chang, K. W.; Jhu, J. G.; Li, Y. Y.; Chen, K. Y.; Yang, C. C.; Chang, W. S.; Chen, L. C. Complete Corrosion Inhibition through Graphene Defect Passivation. *ACS Nano* **2014**, *8*, 443–448.

(36) Lee, W. P.; Routh, A. F. Why Do Drying Films Crack?. *Langmuir* **2004**, *20*, 9885–9888.

(37) Goehring, L.; Conroy, R.; Akhter, A.; Clegg, W. J.; Routh, A. F. Evolution of Mud-Crack Patterns during Repeated Drying Cycles. *Soft Matter* **2010**, *6*, 3562–3567.

(38) Nguyen, D. D.; Suzuki, S.; Kato, S.; To, B. D.; Hsu, C. C.; Murata, H.; Rokuta, E.; Tai, N. H.; Yoshimura, M. Macroscopic, Freestanding, and Tubular Graphene Architectures Fabricated via Thermal Annealing. *ACS Nano* **2015**, *9*, 3206–3214.

(39) Nguyen, A. T.; Lai, W. C.; Tran, V. V.; Nguyen, D. D.; Kan, H. C.; Hsu, C. C. Tubular Graphene Architectures at the Macroscopic Scale: Fabrication and Properties. *Adv. Device Mater.* **2016**, *2*, 23–29.

(40) Rodrigo, S. G.; García-Vidal, F. J.; Martín-Moreno, L. Influence of Material Properties on Extraordinary Optical Transmission through Hole Arrays. *Phys. Rev. B* **2008**, *77*, 075401.

(41) Ferrari, A. C.; Meyer, J. C.; Scardaci, V.; Casiraghi, C.; Lazzeri, M.; Mauri, F.; Piscanec, S.; Jiang, D.; Novoselov, K. S.; Roth, S.; Geim, A. K. Raman Spectrum of Graphene and Graphene Layers. *Phys. Rev. Lett.* **2006**, *97*, 187401.

(342) Roy, P. K.; Ganguly, A.; Yang, W. H.; Wu, C. T.; Hwuang, J. S.; Tai, Y.; Chen, K. H.; Chen, L. C.; Chattopadhyay, S. Edge Promoted Ultrasensitive Electrochemical Detection of Organic Bio-Molecules on Epitaxial Graphene Nanowalls. *Biosensors and Bioelectronics* **2015**, *70*, 137–144.

(43) Malard, L. M.; Pimenta, M. A.; Dresselhaus, G.; Dresselhaus, M. S. Raman Spectroscopy in Graphene. *Physics Reports* **2009**, *473*, 51–87.

- (44) Chen, Y. Z.; Medina, H.; Tsai, H. W.; Wang, Y. C.; Yen, Y. T.; Manikandan, A.; Chueh, Y. L. Low Temperature Growth of Graphene on Glass by Carbon-Enclosed Chemical Vapor Deposition Process and Its Application as Transparent Electrode. *Chem. Mater.* **2015**, *27*, 1646–1655.
- (45) Kohin, M.; Wein, S. J.; Traylor, J. D.; Chase, R. C.; Chapman, J. E. Analysis and Design of Transparent Conductive Coatings and Filters. *Optical Engineering* **1993**, *32*(5), 911-925.
- (46) Jia, L. C.; Yan, D. X.; Yang, Y.; Zhou, D.; Cui, C. H.; Bianco, E.; Lou, J.; Vajtai, R.; Li, B.; Ajayan, P. M.; Li, Z.M. High Strain Tolerant EMI Shielding Using Carbon Nanotube Network Stabilized Rubber Composite. *Adv. Mater. Technol.* **2017**, 1700078.
- (47) Liu, Y.; Tan, J. Frequency Dependent Model of Sheet Resistance and Effect Analysis on Shielding Effectiveness of Transparent Conductive Mesh Coatings. *Progress In Electromagnetics Research* **2013**, *140*, 353-368.
- (48) Lu, Z.; Ma, L.; Tan, J.; Wang, H.; Ding, X. Graphene, Microscale Metallic Mesh, and Transparent Dielectric Hybrid Structure for Excellent Transparent Electromagnetic Interference Shielding and Absorbing. *2D Mater.* **2017**, *4*, 025021.
- (49) Zhang, J.; Yang, Y.; Lou, J. Investigation of Hexagonal Boron Nitride as An Atomically Thin Corrosion Passivation Coating in Aqueous Solution. *Nanotechnology* **2016**, *27*, 364004.
- (50) Zhu, Y. X.; Duan, C. Y.; Liu, H. Y.; Chen, Y. F.; Wang, Y. Graphene Coating for Anti-Corrosion and The Investigation of Failure Mechanism. *J. Phys. D: Appl. Phys.* **2017**, *50*, 114001.
- (51) Prasai, D.; Tuberquia, J. C.; Harl, R. R.; Jennings, G. K.; Bolotin, K. I. Graphene: Corrosion-Inhibiting Coating. *ACS Nano* **2012**, *6*, 1102-1108.

